

# Two dimensional sub-wavelength topological dark state lattices

D. Burba<sup>1</sup> and G. Juzeliūnas<sup>1</sup>

<sup>1</sup>*Institute of Theoretical Physics and Astronomy, Faculty of Physics,  
Vilnius University, Saulėtekio 3, LT-10257, Vilnius, Lithuania*

We present a general framework for engineering two-dimensional (2D) sub-wavelength topological optical lattices using spatially dependent atomic dark states in a  $\Lambda$ -type configuration of the atom-light coupling. By properly designing the spatial profiles of the laser fields inducing coupling between the atomic internal states, we show how to generate sub-wavelength Kronig-Penney-like geometric scalar potential accompanied by narrow and strong patches of the synthetic magnetic field localized in the same areas as the scalar potential. These sharply peaked magnetic fluxes are compensated by a smooth background magnetic field of opposite sign, resulting in zero net flux per unit cell while still enabling topologically nontrivial band structures. Specifically, for sufficiently narrow peaks, their influence is minimum, and the behavior of the system in a remaining smooth background magnetic field resembles the Landau problem, allowing for the formation of nearly flat energy bands with unit Chern numbers. Numerical analysis confirms the existence of ideal Chern bands and the robustness of the topological phases against non-adiabatic effects and losses. This makes the scheme well-suited for simulating quantum Hall systems and fractional Chern insulators in ultracold atomic gases, offering a new platform for exploring strongly correlated topological phases with high tunability.

## I. INTRODUCTION

Ultracold atoms represent a flexible platform for simulating topological and many-body phenomena of condensed matter and high-energy physics [1–5]. The use of atomic dark states offers new possibilities for such simulations. The dark states are long-lived superpositions of atomic internal ground states immune to atom-light coupling [6, 7]. Making the dark states position-dependent, one can create unconventional optical lattices or generate a synthetic magnetic field for ultracold atoms adiabatically following the dark states [8, 9]. In particular, using this method, one can create a one-dimensional (1D) array of sub-wavelength barriers [10–14], thus providing novel optical lattices that were realized experimentally [15, 16]. Recently, two-dimensional (2D) dark-state lattices were also considered [17, 18]. It was demonstrated that in addition to the geometric scalar potential, the dark state atoms can also be affected by a geometric vector potential corresponding to a non-zero magnetic field. The magnetic flux produced in this way is staggered [17], but can have features of the non-staggered flux for a very specific set of parameters [18].

Here we provide a general description of 2D topological dark state lattices elucidating an interplay with the sub-wavelength lattices. In particular, we demonstrate that one can create a topological 2D Kronig-Penney like lattice which contains periodically distributed narrow peaks of strong scalar potential and strong non-staggered magnetic field, the latter located at the same positions as the peaks of the scalar potential. Away from these sub-wavelength patches of the strong magnetic field, there is a smooth magnetic field of the opposite sign, compensating for the former peaks, so the total magnetic flux over an elementary cell is zero. Nevertheless, the system supports topological phases due to the flux variation over a unit cell, involving large areas of smooth magnetic

field. In particular, as the width of the subwavelength peaks of the magnetic fluxes becomes sufficiently small, their influence diminishes and the problem reduces to the motion of the particle in a nearly uniform background field akin to the Landau problem for a particle moving in a constant magnetic field. This work paves the way for experimental exploration of topological phases in 2D sub-wavelength dark-state optical lattices, offering new possibilities for simulating quantum Hall systems, fractional Chern insulators and related strongly correlated phases.

The paper is organised as follows. In the next Section we introduce the  $\Lambda$  scheme of the atom-light coupling and define the dark states which are immune to the atom-light coupling. Section III provides the general description of adiabatic motion of the dark state atoms affected by the geometric scalar and vector potential, as well as the corresponding magnetic field. Section IV considers specific light fields for the  $\Lambda$  scheme providing a 2D sub-wavelength topological lattice for the atomic motion in the dark state manifold. The concluding Sec. V summarizes the findings.

## II. FORMULATION

### A. Hamiltonian

Let us consider atoms in the  $\Lambda$  configuration of energy levels involving two ground states  $|1\rangle$  and  $|2\rangle$  and an excited state  $|e\rangle$  depicted in Fig. 1(a). Both ground states are resonantly (or nearly resonantly with a single photon detuning  $\Delta$ ) coupled to the same excited state  $|e\rangle$  by laser fields characterized by the Rabi frequencies  $\Omega_1$  and  $\Omega_2$ . The Rabi frequencies  $\Omega_1 \equiv \Omega_1(\mathbf{r})$  and  $\Omega_2 \equiv \Omega_2(\mathbf{r})$  are generally position-dependent, as shown in Fig. 1(b), but this  $\mathbf{r}$ -dependence will be mostly kept implicit. Ap-

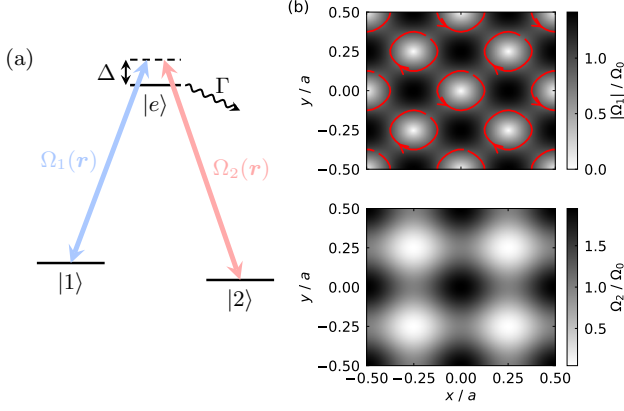


FIG. 1. (a) The Lambda scheme of the atom-light coupling. Two laser fields characterized by Rabi frequencies  $\Omega_1$  and  $\Omega_2$  couple resonantly (or nearly resonantly with a single photon detuning  $\Delta$ ) two atomic ground states  $|1\rangle$  and  $|2\rangle$  to a common excited state  $|e\rangle$ . (b) The position dependence of the modulus of Rabi frequencies  $\Omega_1$  and  $\Omega_2$  given by Eqs. (25)-(26) for  $\epsilon = 1$  and  $\nu = 0.95$ . Arrows indicate the direction of the phase winding of  $\Omega_1$  around its zero points.

plying the rotating wave approximation (RWA) [6], the Hamiltonian describing the atom-light coupling is:

$$\hat{V}/\hbar = \left(-\Delta - \frac{i}{2}\Gamma\right) |e\rangle \langle e| + \sum_{j=1}^2 \left(\frac{\Omega_j}{2} |e\rangle \langle j| + \text{H.c.}\right). \quad (1)$$

where an imaginary contribution  $-i\Gamma/2$  is added to the energy of the excited state to describe its decay at the rate  $\Gamma$ .

### B. Dark and bright state basis

The atom-light Hamiltonian (1) can be represented in term of the excited and bright states

$$\hat{V}/\hbar = \left(-\Delta - \frac{i}{2}\Gamma\right) |e\rangle \langle e| + \frac{\Omega}{2} \left(|e\rangle \langle \tilde{B}| + |\tilde{B}\rangle \langle e|\right), \quad (2)$$

where the bright state  $|\tilde{B}\rangle$  is a superposition of the atomic ground states  $|1\rangle$  and  $|2\rangle$  directly coupled to the excited state  $|e\rangle$ :

$$|\tilde{B}\rangle = \frac{1}{\Omega} (\Omega_1^* |1\rangle + \Omega_2^* |2\rangle), \quad (3)$$

with

$$\Omega = \sqrt{|\Omega_1|^2 + |\Omega_2|^2} \quad (4)$$

being the total Rabi frequency. The third atomic state is the dark state representing a superposition of ground states orthogonal to the bright state

$$|\tilde{D}\rangle = \frac{1}{\Omega} (\Omega_2 |1\rangle - \Omega_1 |2\rangle). \quad (5)$$

Both dark and bright states are position-dependent atomic dressed states. The spatial variation of these states comes from the position-dependence of the Rabi frequencies  $\Omega_1(\mathbf{r})$  and  $\Omega_2(\mathbf{r})$ .

The dark state is not featured in  $\hat{V}$ , so it is not affected by the atom-light coupling and is characterized by zero eigenenergy, i.e.,  $\hat{V}|\tilde{D}\rangle = 0$ .

The dark and bright states can be defined up to a (position-dependent) phase factor. The use of a different set of dark and bright states corresponds to another gauge choice. It is convenient to use the dark and bright states  $|D\rangle$  and  $|B\rangle$  expressed in terms of a relative Rabi frequency  $\zeta = \Omega_1/\Omega_2$ :

$$|D\rangle \equiv \frac{|\Omega_2|}{\Omega_2} |\tilde{D}\rangle = \frac{|1\rangle - \zeta |2\rangle}{\sqrt{1 + |\zeta|^2}}, \quad (6)$$

$$|B\rangle \equiv \frac{|\Omega_2|}{\Omega_2^*} |\tilde{B}\rangle = \frac{1}{\sqrt{1 + |\zeta|^2}} (\zeta^* |1\rangle + |2\rangle). \quad (7)$$

In the present paper we will concentrate of the situation where  $\Omega_2$  is real, so the two sets of dark and bright states coincide up to a sign of  $\Omega_2$ .

For a sufficiently large single photon detuning,  $\Delta \gg \Omega$ , one can adiabatically eliminate the excited state  $|e\rangle$ . Specifically, applying the Schrieffer-Wolff transformation (see e.g. the Supplementary material of ref. [19]), the effective Hamiltonian describing the atomic dynamics in the ground state manifold is

$$\hat{V}_{\text{eff}} = \frac{V_0}{4} |\tilde{B}\rangle \langle \tilde{B}| = \frac{V_0}{4} |B\rangle \langle B|, \quad (8)$$

with

$$V_0 = \frac{\Omega^2}{\Delta + i\Gamma/2}, \quad (9)$$

where the real and imaginary parts of  $V_0$  describe, respectively, the light shift and the decay of the bright state. The dark state is characterized by zero eigenenergy also in the projected description  $\hat{V}_{\text{eff}}|\tilde{D}\rangle = 0$ , so the dark state neither decays, nor experiences the light shift, like in the full description involving all three atomic internal states.

### III. ADIABATIC MOTION IN THE DARK STATE MANIFOLD

Including the kinetic energy, the combined internal and center of mass atomic dynamics is described by the Hamiltonian:

$$\hat{H} = \frac{\hat{\mathbf{p}}^2}{2M} + \hat{V}, \quad (10)$$

where  $\mathbf{p} = -i\hbar\nabla$  is the momentum operator,  $M$  is the atomic mass and  $\hat{V}$  is the atom-light coupling Hamiltonian given by Eqs. (1) or (2).

The atomic combined internal and center of mass dynamics is generally described by a multi-component state-vector  $|\psi(\mathbf{r})\rangle$  which can be cast in terms of bare atomic internal states  $|1\rangle$ ,  $|2\rangle$  and  $|e\rangle$ , or alternatively, in the basis of dark, bright and excited states  $|D\rangle \equiv |D(\mathbf{r})\rangle$ ,  $|B\rangle \equiv |B(\mathbf{r})\rangle$  and  $|e\rangle$ :

$$|\psi(\mathbf{r})\rangle = \psi_D(\mathbf{r})|D(\mathbf{r})\rangle + \psi_B(\mathbf{r})|B(\mathbf{r})\rangle + \psi_e(\mathbf{r})|e\rangle, \quad (11)$$

where  $\psi_D(\mathbf{r})$ ,  $\psi_B(\mathbf{r})$  and  $\psi_e(\mathbf{r})$  are wavefunctions for the center of motion of atoms in the corresponding internal states. For a sufficiently large detuning,  $\Delta \gg \Omega$ , one can consider the state vector projected onto the dark and bright state manifolds  $|\psi_{\text{eff}}(\mathbf{r})\rangle = \psi_D(\mathbf{r})|D(\mathbf{r})\rangle + \psi_B(\mathbf{r})|B(\mathbf{r})\rangle$ . The evolution of  $|\psi_{\text{eff}}(\mathbf{r})\rangle$  is then governed by the effective Hamiltonian  $\hat{H}_{\text{eff}}$  which has the form of Eq. (10) with the atom-light operator  $\hat{V}$  replaced by the effective operator  $\hat{V}_{\text{eff}}$  given by Eq. (8). Such an approach has been applied in refs. [18, 20] (with the real valued coupling strength  $V_0$  corresponding to neglect of losses). Our numerical analysis will be based on the dynamics of the complete state-vector  $|\psi(\mathbf{r})\rangle$  governed by the full Hamiltonian  $\hat{H}$  of Eq. (10), and a comparison to the projected dynamics described by  $\hat{H}_{\text{eff}}$  will be discussed. We will see that in the regime where the atoms adiabatically follow the dark state, the complete and projected dynamics governed by the Hamiltonian  $\hat{H}$  and  $\hat{H}_{\text{eff}}$  yield very similar energy spectra (especially for lower energies) even for moderate detuning  $\Delta$ . Interestingly, the effects of losses are also similar using the two approaches, and the reason for this will be elucidated in Sec. IV D.

### A. Adiabatic approximation

When the total Rabi frequency  $\Omega$  greatly exceeds the characteristic energy of the atomic center of mass motion, the atoms adiabatically follow the lossless dark state to a good approximation. The atomic center of mass motion can then be described by the dark-state wavefunction  $\psi_D(\mathbf{r})$  whose evolution is governed by the following Hamiltonian [8, 9, 21, 22]

$$\hat{H}_D = \frac{1}{2M}(-i\hbar\nabla - \mathbf{A})^2 + \phi, \quad (12)$$

where  $\mathbf{A} \equiv \mathbf{A}(\mathbf{r})$  and  $\phi \equiv \phi(\mathbf{r})$  are geometric vector and scalar potentials

$$\mathbf{A} = i\hbar \langle D | \nabla | D \rangle \quad \text{and} \quad \phi = \frac{\hbar^2}{2m} \mathbf{A}_{DB} \cdot \mathbf{A}_{BD}, \quad (13)$$

with

$$\mathbf{A}_{DB} = i\hbar \langle D | \nabla | B \rangle \quad \text{and} \quad \mathbf{A}_{BD} = \mathbf{A}_{DB}^* \quad (14)$$

being the off-diagonal matrix elements of the vector potential associated with the non-adiabatic transitions between the dark and bright states. Note that the Hamiltonian (12) does not contain the dark state energy, as it

equals to zero. Thus the adiabatic following of the dark state is not accompanied with any additional scalar potential due to the position-dependence of the dark state energy, which facilitates simulation of the situation close to the Quantum Hall physics.

The geometric vector and scalar potentials acting on atoms the dark state  $|D\rangle$ , as well as the corresponding magnetic field  $\mathbf{B} = \nabla \times \mathbf{A}$  read [21, 22]

$$\mathbf{A} = \frac{i\hbar}{2} \frac{\zeta^* \nabla \zeta - \zeta \nabla \zeta^*}{1 + |\zeta|^2} = -\hbar \frac{\eta^2}{1 + \eta^2} \nabla S, \quad (15)$$

$$\phi = \frac{\hbar^2}{2m} \frac{\nabla \zeta^* \cdot \nabla \zeta}{(1 + |\zeta|^2)^2} = \frac{\hbar^2}{2m} \frac{\eta^2 (\nabla S)^2 + (\nabla \eta)^2}{(1 + \eta^2)^2}, \quad (16)$$

and

$$\mathbf{B} = i\hbar \frac{1}{(1 + |\zeta|^2)^2} \nabla \zeta^* \times \nabla \zeta = \hbar \frac{(\nabla S) \times \nabla \eta^2}{(1 + \eta^2)^2}, \quad (17)$$

where  $\eta$  and  $S$  are, respectively, the real valued amplitude and the phase of the relative Rabi frequency

$$\zeta = \Omega_1/\Omega_2 = \eta e^{iS}, \quad (18)$$

where  $\eta$  can be positive or negative.

### B. Magnetic flux for periodic atom-light coupling

In what follows the Rabi frequencies  $\Omega_1$  and  $\Omega_2$  and thus the atom-light coupling  $\hat{V}$  are considered to be spatially periodic in the  $\mathbf{e}_x\text{-}\mathbf{e}_y$  plane

$$\Omega_{1,2}(\mathbf{r} + \mathbf{r}_{n,m}) = \Omega_{1,2}(\mathbf{r}) \quad \text{and} \quad \hat{V}(\mathbf{r} + \mathbf{r}_{n,m}) = \hat{V}(\mathbf{r}), \quad (19)$$

with  $\mathbf{r}_{n,m} = n\mathbf{a}_1 + m\mathbf{a}_2$ , where  $\mathbf{a}_1$  and  $\mathbf{a}_2$  are primitive vectors defining the 2D lattice,  $n$  and  $m$  being integers.

Let us first consider the general properties of the vector potential  $\mathbf{A} = \mathbf{A}(\mathbf{r})$  and the corresponding magnetic field  $\mathbf{B} = \mathbf{B}(\mathbf{r})$  for atoms adiabatically following a certain dressed state representing a non-degenerate eigenstate of a spatially periodic atom-light coupling operator  $\hat{V}(\mathbf{r})$ . In the present situation such a dressed state represents the dark state  $|D\rangle = |D(\mathbf{r})\rangle$ , but the same arguments apply to atoms adiabatically following any non-degenerate dressed state corresponding to any spatially periodic atom-light coupling [23]. Atomic dressed states have the lattice periodicity, so the corresponding geometric vector potential is also periodic:  $\mathbf{A}(\mathbf{r} + \mathbf{r}_{n,m}) = \mathbf{A}(\mathbf{r})$ . For this reason the total magnetic flux over an elementary cell is zero:

$$\alpha = \oint_{\text{cell}} \mathbf{A} \cdot d\mathbf{r} = 0. \quad (20)$$

Using the Stokes theorem, the total magnetic flux  $\alpha$  can be represented as:

$$\alpha = \alpha' + \sum_{\text{singul}} \oint \mathbf{A} \cdot d\mathbf{r}, \quad (21)$$

where the first term is the flux due to the actual (continuous) magnetic field  $\mathbf{B} = \nabla \times \mathbf{A}$ :

$$\alpha' = \iint_{\text{cell}} \mathbf{B} \cdot d\mathbf{S}. \quad (22)$$

The second term in Eq. (21) involves integration around all (gauge-dependent) singular points of the vector potential. From Eqs. (20)-(21) it follows that the actual magnetic flux  $\alpha'$  over the elementary cell is determined by the singularities of the vector potential [18, 23]:

$$\alpha' = - \sum \oint_{\text{singul}} \mathbf{A} \cdot d\mathbf{r}. \quad (23)$$

Note that, if the atom-light coupling involves two atomic internal states, the eigenstates of such a two-level system (the dressed states) can be parameterized by the azimuthal and polar angles of the Bloch sphere. Such dressed states are not single-valued in the south or north poles of the Bloch sphere, at which the vector potential for the adiabatic motion in one of the dressed states can be singular [8]. By properly choosing the atom-light coupling, one can thus get a non-zero magnetic flux over a plaquette  $\alpha'$  equal to an integer number of the Dirac quanta  $2\pi\hbar$  [23–25]. The non-zero magnetic flux over a plaquette  $\alpha'$  can also be created for a more general situation of any spin or quasi-spin (not necessarily quasi-spin 1/2) adiabatically following an effective magnetic field [23].

The situation is different for atoms adiabatically following the dark state of the  $\Lambda$  scheme. In fact, the dark state  $|\tilde{D}\rangle$  given by Eq. (5) is fully determined by the Rabi frequencies  $\Omega_1$  and  $\Omega_2$  and thus is single valued, as long as the total Rabi frequency  $\Omega$  is non-zero, i.e. as long as the dark state is not degenerate with the bright state and thus the adiabatic concept is applicable. As a result, atoms adiabatically following the dark state are affected by the vector potential which does not have singularities and thus the magnetic flux over a plaquette is zero:

$$\alpha' = 0. \quad (24)$$

The same holds for the dark state  $|D\rangle$  given by Eq. (6), corresponding to another gauge, as the gauge transformation can not change the measurable magnetic flux  $\alpha'$ . Thus one can not create a non-staggered magnetic flux for the dark state atoms of the  $\Lambda$  scheme within the adiabatic approach. Yet, as we will see later, the non-staggered magnetic field can be composed of a smooth background magnetic field and a set of narrow tubes of a strong magnetic field with an opposite sign compensating the background flux. If the flux tubes are narrow enough, they will not influence significantly the atomic motion in the uniform background magnetic flux. Thus one arrives effectively at a situation close to motion of a particle in the uniform magnetic field.

## IV. ATOM-LIGHT COUPLING

### A. Coupling scheme

The situation described above can be implemented using the  $\Lambda$  scheme with the following Rabi frequencies of the atom-light coupling depicted in Fig. 1(b):

$$\Omega_1(\mathbf{r}) = \Omega_0 [\sin(k(x+y)) - i \sin(k(x-y))] \quad (25)$$

and

$$\Omega_2(\mathbf{r}) = \epsilon \Omega_0 \left[ 1 + \frac{\nu}{2} \cos(2kx) + \frac{\nu}{2} \cos(2ky) \right]. \quad (26)$$

The experimental feasibility of this setup will be discussed later in the paper.

The Rabi frequencies given by Eqs. (25)-(26) accommodate the schemes considered in refs. [17] and [18]. For  $\nu = 0$ , the scheme reduces to a situation analyzed in ref. [17]. In particular it was demonstrated, that for  $\nu = 0$  and  $\epsilon \ll 1$  one can create a 2D Kronig-Penney lattice representing a set of 2D subwavelength potential peaks affected by a staggered magnetic flux [17]. On the other hand, ref. [18] concentrated on the situation where  $\epsilon = 1$  and  $\nu = 1$  for creating topological bands.

### B. Symmetries of Hamiltonian

The atom-light coupling operator  $\hat{V}(\mathbf{r})$  characterized by the Rabi frequencies  $\Omega_{1,2}(\mathbf{r})$ , Eqs. (25)-(26), is invariant with respect to spatial shifts by the lattice vectors

$$\mathbf{a}_1 \equiv \mathbf{a}_x = a\mathbf{e}_x \quad \text{and} \quad \mathbf{a}_2 \equiv \mathbf{a}_y = a\mathbf{e}_y, \quad (27)$$

where

$$a = 2\pi/k \quad (28)$$

is the lattice constant, with  $\mathbf{e}_x$  and  $\mathbf{e}_y$  being the unit Cartesian vectors. Additionally, as in the case of  $\nu = 0$  [17], one has

$$\begin{aligned} \Omega_1(\mathbf{r} + \mathbf{a}_x/2) &= \Omega_1(\mathbf{r} + \mathbf{a}_y/2) = -\Omega_1(\mathbf{r}), \\ \Omega_2(\mathbf{r} + \mathbf{a}_x/2) &= \Omega_2(\mathbf{r} + \mathbf{a}_y/2) = \Omega_2(\mathbf{r}). \end{aligned} \quad (29)$$

Hence the Hamiltonian  $\hat{H}$  is invariant with regards to an operation

$$\hat{T}_{\mathbf{a}_u/2} = \hat{U} \exp\left(\frac{i\mathbf{a}_u \cdot \hat{\mathbf{p}}}{2\hbar}\right) \quad (u = x, y) \quad (30)$$

involving spatial translations by a half of the lattice vectors accompanied by a self-inverse (involutory) unitary operation  $\hat{U}$  [17]:

$$\hat{U} = |1\rangle\langle 1| - |2\rangle\langle 2| - |0\rangle\langle 0|, \quad \text{with} \quad \hat{U}^2 = \hat{I}. \quad (31)$$

The dark state is not affected by such a combined shift:  $\hat{T}_{x,y}|\tilde{D}\rangle = |\tilde{D}\rangle$ , so the geometric vector and scalar potentials  $\mathbf{A}(\mathbf{r})$  and  $\phi(\mathbf{r})$  have a periodicity  $a/2$  equal to half of the original lattice constant along the  $x$  and  $y$  axes:

$$\mathbf{A}(\mathbf{r} + \mathbf{a}_u/2) = \mathbf{A}(\mathbf{r}), \quad \phi(\mathbf{r} + \mathbf{a}_u/2) = \phi(\mathbf{r}) \quad (32)$$

with  $u = x, y$ . As the Hamiltonian  $\hat{H}$  commutes with the combined shift operators  $\hat{T}_{\mathbf{a}_u/2}$ , these operators share a common set of eigenstates

$$|\psi_s^{(\mathbf{q})}(\mathbf{r})\rangle = e^{i\mathbf{q}\cdot\mathbf{r}} |u_s^{(\mathbf{q})}(\mathbf{r})\rangle, \quad (33)$$

with

$$\hat{H} |\psi_s^{(\mathbf{q})}(\mathbf{r})\rangle = E_s(\mathbf{q}) |\psi_s^{(\mathbf{q})}(\mathbf{r})\rangle, \quad (34)$$

where  $|u_s^{(\mathbf{q})}(\mathbf{r})\rangle$  is a part invariant with respect to the combined shift by a half of the lattice constant

$$\hat{T}_{\mathbf{a}_u/2} |u_s^{(\mathbf{q})}(\mathbf{r})\rangle = |u_s^{(\mathbf{q})}(\mathbf{r})\rangle. \quad (35)$$

Here  $s$  labels the Bloch bands characterized by the energy  $E_s(\mathbf{q})$  and quasi-momentum  $\mathbf{q} = q_x \mathbf{e}_x + q_y \mathbf{e}_y$ , the latter covering an extended Brillouin zone which is twice larger in each Cartesian direction:  $-2\pi/a \leq q_{x,y} < 2\pi/a$ . In calculating the energy spectrum of the system we will look for the eigenstates of the form of Eq. (33). Note that describing the atom-light coupling in terms of the projected operator  $\hat{V}_{\text{eff}}$  given by Eq. (8), the operator  $\hat{U}$  featured in the combined shift operator (30) reduces to the  $\sigma_z$ , as in ref. [18].

Consider next the time reversal operation  $\mathcal{T}$  involving the complex conjugation  $K$  and a spatial shift by a half of the lattice constant along both axes simultaneously:  $\mathbf{r} \rightarrow \mathbf{r} + (\mathbf{a}_x + \mathbf{a}_y)/2$ :

$$\mathcal{T} = \exp\left(\frac{i(\mathbf{a}_x + \mathbf{a}_y) \cdot \hat{\mathbf{p}}}{2\hbar}\right) K. \quad (36)$$

Without including the excited state decay ( $\Gamma = 0$ ), the time reversal transformation flips the sign of the parameter  $\nu$  in the Hamiltonian  $\hat{H} \equiv \hat{H}_\nu$ :

$$\mathcal{T}: \hat{H}_\nu \rightarrow \hat{H}_{-\nu}, \quad (37)$$

so the Hamiltonian  $\hat{H} = \hat{H}_\nu$  breaks the time reversal symmetry unless  $\nu = 0$ . Generally 2D systems without the time reversal symmetry are characterized by integer Chern numbers describing the Quantum Hall response [26, 27]. Thus for  $\nu \neq 0$  the energy bands of the system can be characterized by non-zero Chern numbers  $c$  which reverse the sign  $c \rightarrow -c$  by changing  $\nu \rightarrow -\nu$ , leading to reversal of the currents in the chiral edge states.

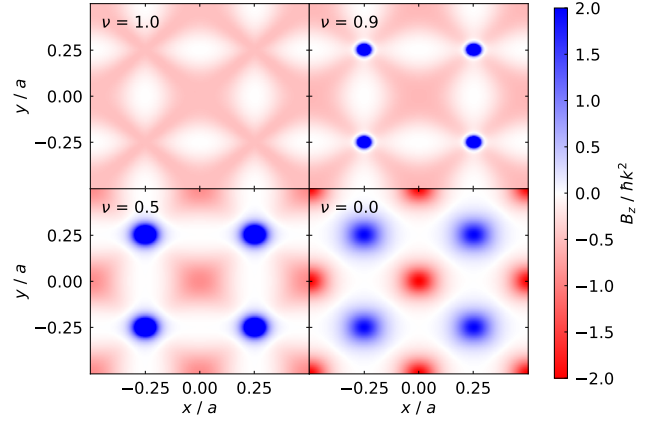


FIG. 2. Spatial dependence of the magnetic field  $B_z$  for  $\epsilon = 1$  and  $\nu = \{1, 0.9, 0.5, 0\}$  when  $\Delta = 2000E_R$ ,  $\Gamma = 1000E_R$  and  $\Omega_0 = 2000E_R$ . Note that the magnetic field around the narrow peaks are far beyond the range of their values shown. Specifically, the largest  $|B_z|$  and  $\phi$  are equal approximately to  $\{1, 400, 16, 4\} \hbar k^2$  and  $\{1, 400, 16, 4\} E_R$  for  $\nu = \{1, 0.9, 0.5, 0\}$ , respectively. The geometric scalar potential  $\phi$  behaves very similar to the absolute value of  $B_z$ .

### C. Effective magnetic field and scalar potential

#### 1. Plots

Figure 2 shows the amplitude  $B_z$  of the effective magnetic field  $\mathbf{B} = B_z \mathbf{e}_z$  for  $\epsilon = 1$  and different values of  $\nu \geq 0$ . For  $\nu = 0$  the positive and negative values of  $B_z$  are distributed in the same way, but are shifted with respect to each other by  $(\mathbf{a}_x + \mathbf{a}_y)/2$  or  $(\mathbf{a}_x - \mathbf{a}_y)/2$ , i.e. by half of a lattice constant  $a$  simultaneously along both Cartesian axes  $x$  and  $y$ . Increasing  $\nu$ , the positive magnetic field spreads out, whereas the negative magnetic field becomes concentrated in smaller spots with a larger strength, so that the total magnetic flux over an elementary cell sums to zero, as required by Eq. (24). Note that for  $\nu \rightarrow \pm 1$ , the flux tubes become infinitely narrow and thus reduce to the 2D Dirac delta functions which are not visible in Fig. 2 for  $\epsilon = \nu = 1$ . Outside the areas of the narrow peaks, the magnetic field is the most uniform for  $\epsilon = 1$  and  $\nu \rightarrow 1$ , as one can see in Fig. 3. Reversing the sign of  $\nu$ , the magnetic field remains distributed the same as in Fig. 2 subject to the spatial shift by  $(\mathbf{a}_x + \mathbf{a}_y)/2$  or  $(\mathbf{a}_x - \mathbf{a}_y)/2$ , as well as the reversal of the sign of the magnetic field. Therefore in what follows we will concentrate mostly on the situation where  $\nu \geq 0$ . The geometric scalar potential  $\phi$  behaves very similarly to the absolute value of the magnetic field  $|B_z|$  and has the same kind of narrow peaks, as follows from Eqs. (41) and (43) presented below.



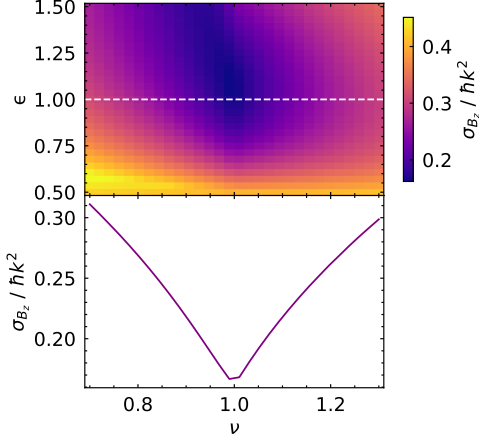


FIG. 3. Dependence of the standard deviation of magnetic field  $B_z$  on  $\epsilon$  and  $\nu$  (upper plot), as well as on  $\nu$  for  $\epsilon = 1$  (lower plot). Other parameters are  $\Delta = 2000E_R$ ,  $\Gamma = 1000E_R$ ,  $\Omega_0 = 2000E_R$ . For  $\nu \neq 1$  we have eliminated narrow peaks of the magnetic field by cutting the magnetic field exceeding the maximum of the absolute value of  $B_z$  corresponding to  $\epsilon = 1$  and  $\nu = 0$ . The standard deviation of the scalar potential  $\phi$  is characterized by nearly identical plots.

## 2. Analysis in a vicinity of zero points of $\Omega_1(\mathbf{r})$

The appearance of narrow magnetic flux tubes featured in Fig. 2 as  $\nu$  is close to the unity, can be understood from the following arguments. The Rabi frequency  $\Omega_1(\mathbf{r})$  given by Eq. (25) equals to zero when  $x + y = na/2$  and  $x - y = ma/2$ , where  $n$  and  $m$  are integers. Around these zero points of  $\Omega_1(\mathbf{r})$ , one can write  $x + y = na/2 + \rho \cos \varphi$  and  $x - y = ma/2 + \rho \sin \varphi$  with  $\rho \ll a$ . Thus the relative Rabi frequency  $\zeta$  given by Eq. (18) reads up to the leading terms in the radial deviation  $\rho$ :

$$\zeta \approx \eta_\rho e^{\mp i\varphi}, \quad \text{with} \quad \eta_\rho = (-1)^n \frac{k\rho}{\epsilon(1 \pm \nu \mp 2ck^2\rho^2)}, \quad (38)$$

where the sign  $\mp 1 = (-1)^{n+m}$  corresponds to the phase winding of the Rabi frequency  $\Omega_1(\mathbf{r})$ , represented by arrows in Fig. 1(b). In the denominator of  $\eta_\rho$ , we have retained a term quadratic in  $\rho$ , because the constant term  $1 \pm \nu$  becomes vanishingly small as  $\nu \rightarrow \mp 1$ . Using Eq. (15) for  $\mathbf{A}$  with  $\zeta$  given by Eq. (38), the magnetic flux over the radius  $\rho$  is

$$\alpha_\rho = - \oint_\rho \mathbf{A} \cdot d\mathbf{r} = \pm 2\pi\hbar \frac{\eta_\rho^2}{1 + \eta_\rho^2}. \quad (39)$$

If  $\nu \neq \mp 1$ , the magnetic flux  $\alpha_\rho$  is zero for  $\rho = 0$ . Subsequently, the flux increases with  $\rho$  and approaches the maximum flux value equal to  $\pm 2\pi\hbar$  as  $\eta_\rho^2 \gg 1$ , where  $2\pi\hbar$  is the Dirac flux quantum. A characteristic radius  $\rho_0$  over which the magnetic field is concentrated can be estimated

by taking  $\eta_{\rho_0}^2 \approx 1$ , which gives for  $\epsilon|1 \pm \nu| \ll 1$ :

$$k\rho_0 = \epsilon|1 \pm \nu|. \quad (40)$$

Consider next the synthetic magnetic field and the geometric scalar potential around the zero points of  $\Omega_1(\mathbf{r})$  with  $\epsilon|1 \pm \nu| \ll 1$ , where  $|\Omega_2(\mathbf{r})|$  is minimum (see Fig. 1(b)), so the changes of the relative Rabi frequency  $\zeta = \Omega_1/\Omega_2$  generating the geometric potentials are maximum. Substituting Eq. (38) into Eqs. (16), one has:

$$B_z = \pm 2\hbar k^2 f(\rho), \quad \phi = 2E_R f(\rho), \quad (41)$$

where

$$E_R = \frac{\hbar^2 k^2}{2m} \quad (42)$$

is the recoil energy and

$$f(\rho) = \frac{k^2 \rho_0^2}{(k^2 \rho^2 + k^2 \rho_0^2)^2}, \quad (43)$$

with  $\rho_0$  as in Eq. (40). Thus close to the zero points of  $\Omega_1(\mathbf{r})$  with  $\epsilon|1 \pm \nu| \ll 1$ , the effective magnetic field  $B_z$  and geometric scalar potential  $\phi$  have the spatial dependence characterized by the same function  $f(\rho)$ , like the geometric potentials produced by vortex light beams [28]. As  $k\rho_0 \ll 1$ , the function  $f(\rho)$  describes narrow and large peaks of the magnetic field and the scalar potential with the radius  $\rho_0 = \epsilon|1 \pm \nu|/k$  much smaller than the lattice constant  $a = 2\pi/k$ . For example, if  $\epsilon = \nu = 1$ , the condition  $\epsilon|1 \pm \nu| \ll 1$  is fulfilled for the lower sign (even  $n + m$ ) corresponding to the minima of  $|\Omega_2(\mathbf{r})|$  in Fig. 1(b). This provides narrow negative peaks of the magnetic field at the zero points of  $\Omega_1(\mathbf{r})$  with even  $n + m$ , as one can see in Fig. 2. On the other hand, if  $\epsilon \ll 1$ , the narrow peaks of the magnetic field and the scalar potential can be formed also for the time-reversal case with  $\nu = 0$  [17]. In such a situation, the narrow magnetic fluxes proportional to  $\mp 1 = (-1)^{n+m}$  alternate their sign depending on the parity of  $n + m$ , and there is no smooth background magnetic flux, as illustrated in Fig. 4. It is instructive that width of the function  $f(\rho)$  defining the magnetic field and the geometric scalar potential in Eqs. (41)-(43), is proportional to  $\rho_0$  whereas the height of the peaks goes as  $1/\rho_0^2$ . Therefore the function  $f(\rho)$  becomes proportional to the 2D Dirac delta function as  $k\rho_0 \rightarrow 0$ . Note that for 1D dark-state lattices one can also produce the subwavelength potential barriers of the width  $x_0$  and the height proportional  $1/x_0^2$  [10, 11]. Yet the area over such a 1D barrier is proportional to  $1/x_0$  and thus increases to infinity as  $x_0$  goes to zero, making the tunneling over the 1D subwavelength dark-state barriers fully suppressed.

For  $\nu = \mp 1$ , Eq. (38) yields  $\eta_\rho \propto 1/\rho$ , so the magnetic flux  $\alpha_\rho$  given by Eq. (39) reaches a finite value  $\pm 2\pi\hbar$  as  $\rho \rightarrow 0$ . Hence, the narrow magnetic fluxes, featured for  $\epsilon|1 \pm \nu| \ll 1$ , reduce to the Aharonov-Bohm type singularities as  $\nu = \mp 1$ . Yet, in practice one can not have the

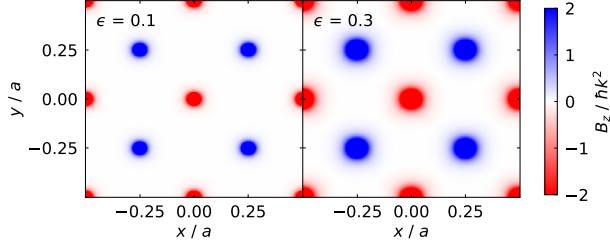


FIG. 4. Spatial dependence of the magnetic field  $B_z$  for  $\nu = 0$  and  $\epsilon = \{0.1, 0.3\}$  when  $\Delta = 2000E_R$ ,  $\Gamma = 1000E_R$  and  $\Omega_0 = 2000E_R$ . Note that the magnetic field around the narrow peaks are far beyond the range of their values shown. Specifically, the largest  $|B_z|$  are equal approximately to  $\{400, 44.4444\} \hbar k^2$  for  $\epsilon = \{0.1, 0.3\}$ . The geometric scalar potential  $\phi$  looks very similar to the absolute value of  $B_z$ .

perfect tuning; even a tiny deviation from  $\nu = \mp 1$  makes the magnetic flux somewhat extended around  $\rho = 0$ , removing the perfect Aharonov-Bohm singularity. On the other hand, if  $\nu = \mp 1$  and hence  $\rho_0 = 0$ , the dark and bright states are degenerate at  $\rho = 0$ . Strictly speaking, in this region the adiabatic approach is no longer applicable and one can not use the concept of the geometric vector potential and magnetic field, as well as the geometric scalar potential. Let us consider this issue in more detail.

### 3. Applicability of adiabaticity

The applicability of adiabaticity can be characterized by the ratio  $\gamma(\rho)$  between the scalar potential  $\phi$  (describing the non-adiabatic transitions) and the energy difference between the dark and bright states  $E_{BD} \approx \Omega^2/\Delta$ , with  $\Omega \equiv \Omega(\mathbf{r})$ . In a vicinity of  $\rho = 0$ , the energy difference reads

$$E_{BD} \approx \Omega_0^2 k^2 (\rho^2 + \rho_0^2) / \Delta. \quad (44)$$

Using also Eqs. (41)-(43) for  $\phi$ , the ratio  $\gamma(\rho)$  is

$$\gamma(\rho) = \frac{\phi}{E_{BD}} \approx \frac{\rho_{c1}^4 \rho_0^2}{(\rho^2 + \rho_0^2)^3}, \quad (45)$$

with

$$k^4 \rho_{c1}^4 = \frac{2E_R \Delta}{\Omega_0^2}, \quad (46)$$

where  $k\rho_{c1} \ll 1$ , as the recoil energy  $E_R$  is usually several orders of magnitude smaller than the Rabi frequency  $\Omega_0$ , while the detuning  $\Delta$  can be of the order of  $\Omega_0$ . The ratio  $\gamma(\rho)$  is maximum for  $\rho = 0$ , where

$$\gamma(\rho)|_{\rho=0} = \gamma_0 = \rho_{c1}^4 / \rho_0^4. \quad (47)$$

If the radius  $\rho_0$  describing the width of the effective magnetic field and the geometric scalar potential is equal to

$\rho_{c1}$ , i.e.  $\rho_0 = \rho_{c1}$ , the ratio  $\gamma_0$  equals to the unity, and the non-adiabatic transitions become significant in a vicinity of  $\rho = 0$ . The distance  $\rho_0 = \rho_{c1}$  thus represents the first border line when the non-adiabatic transitions and losses start to be important. By further decreasing  $\rho_0$  one reaches the point  $\rho_0 = \rho_{c2} < \rho_{c1}$  for which  $\gamma(\rho) = 1$  at  $\rho = \rho_0 = \rho_{c2}$ . Using Eq. (45), the latter radius is

$$\rho_{c2} = 2^{-3/4} \rho_{c1} \approx 0.6 \rho_{c1}. \quad (48)$$

In this way, reducing the  $\rho_0$  to  $\rho_0 = \rho_{c2}$ , the non-adiabatic transitions become important for the area  $\rho < \rho_{c2}$ , in which the scalar potential and the magnetic field are concentrated. In this region the atoms no longer adiabatically follow the dark state and thus no longer feel the scalar potential and the magnetic field. The laser fields are then too weak to induce a sufficient splitting between the dark and bright states and also to provide substantial losses. In this “gray area” with  $\rho < \rho_{c2}$ , the center of mass evolution does not alter the atomic internal state in any considerable way. In fact, for  $\rho > \rho_0 = \rho_{c2}$  the atomic dark state is close to the internal state  $|2\rangle$ , and the atoms remain in this state also for  $\rho < \rho_{c2}$  where the Rabi frequency  $\Omega$  is too small to change the atomic internal state. In the limit where  $\nu \rightarrow \mp 1$  both critical radii  $\rho_{c1}$  and  $\rho_{c2}$  go to zero, so there is no issue with the non-adiabaticity due to the infinitely narrow spots of the magnetic field and the vector potential at  $\rho = 0$ .

### D. Spectrum

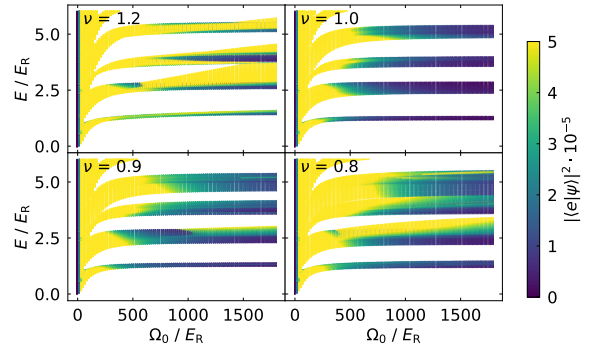


FIG. 5. Dependence of eigenenergies  $E$  on the amplitude  $\Omega_0$  of the Rabi frequency for the four lowest Bloch bands belonging to the dark state manifold for  $\epsilon = 1$  and  $\nu = \{1.2, 1.0, 0.9, 0.8\}$ , with  $\Delta = 2000E_R$  and  $\Gamma = 1000E_R$ . The calculations have been done using the full Hamiltonian (10) with the atom-light coupling operator  $\hat{V}$  involving all three atomic internal states. Colors correspond to the excited state population of the eigenstates  $|\langle e|\psi\rangle|^2$  due to non-adiabatic effects.

Figure 5 shows the dependence of the energy spectrum of the system on the atom-light coupling strength  $\Omega_0$  when  $\epsilon = 1$  and  $\nu$  is close to the unity. The plots include the four lowest bands of the dark state manifold;

the colors indicate the population for the corresponding energy of the lossy excited state due to non-adiabatic effects. The excited state population is proportional to the imaginary part of the energy and is thus a measure of losses. For  $\nu = 1$  the excited state population is very close to zero as long as  $\Omega_0$  is not too small and thus the adiabatic following of the dark state holds to a good approximation. As  $\nu$  deviates from the unity, the excited state population increases, especially in the upper parts of the energy spectrum. This is because departure from  $\nu = 1$  leads to formation of the finite-width peaks of magnetic fluxes and geometric scalar potential  $\phi$  around the zero points of  $\Omega_1$  corresponding to odd  $n + m$ , as one can see in Fig. 2. Yet, according to Eq. (13), the geometric potential  $\phi$  is proportional to  $|\mathbf{A}_{\text{DB}}|^2$ , where  $\mathbf{A}_{\text{DB}}$  is the off diagonal matrix element of the vector potential responsible for the non-adiabatic coupling between the dark and bright states. Hence the non-adiabatic coupling is significant around the peaks of the scalar potential and magnetic field.

The calculations presented in Fig. 5 have been carried out using the complete Hamiltonian (10) with the atom-light coupling operator  $\hat{V}$  [given by Eqs. (1), (25) and (26)] involving all three atomic internal states. We have checked that almost the same energy spectrum and the same losses are obtained replacing the full atom-light coupling operator  $\hat{V}$  by the projected operator  $\hat{V}_{\text{eff}}$  [given by Eq. (8)] acting on the manifold of the dark and bright states. This can be understood from the fact, that for a sufficiently large total Rabi frequency  $\Omega$  the atoms adiabatically follow the dark state, so the atomic dynamics is determined exclusively by the position-dependence of the dark state defining the geometric vector and scalar potentials  $\mathbf{A}$  and  $\phi$  in Eqs. (13)-(14). In such an adiabatic dynamics, the losses originate mostly from the spatial areas close to the zero points of the Rabi frequency  $\Omega \equiv \Omega(\mathbf{r})$  where the adiabaticity holds weaker. Yet close to its zero points the total Rabi frequency  $\Omega(\mathbf{r})$  is so small that the condition  $\Omega(\mathbf{r}) \ll \Delta$  holds even if the detuning  $\Delta$  is equal to the Rabi frequency  $\Omega_0$ , as it is the case for the plots presented in Fig. 5. As a result, the projected description works well to describe the losses.

For  $\nu$  close to the unity and large enough values of  $\Omega_0$ , the energy bands shown in Fig. 5 are nearly equally spaced and have non-trivial topology characterized by unit Chern numbers  $c = 1$  [29], as for the perfect tuning when  $\nu = 1$  [18]. The ratio of the width of individual bands to the band gap is the smallest for  $\nu = 1$  and increases with the deviation from this value. This can be understood from the fact that for  $\nu \rightarrow 1$  both the magnetic field and the scalar potential are the most uniform (see Fig. 3), so the situation is the closest to the Landau problem of motion of a particle in the uniform magnetic field and uniform scalar potential, where the Bloch bands are flat. As illustrated in Fig. 6, for  $\nu$  sufficiently close to the unity ( $\nu = 1, 0.98$  and  $0.95$ ), the lowest energy Bloch state with zero quasi-momentum  $\mathbf{q} = 0$  has density holes centered at the zero points of  $\Omega_1$  corresponding to even

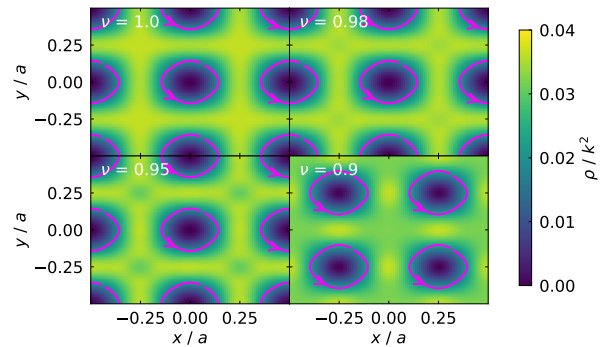


FIG. 6. Spatial dependence of the total atomic population  $\rho$  in the lowest energy Bloch state with zero quasi-momentum  $\mathbf{q} = 0$  for  $\epsilon = 1.0$ ,  $\nu = \{1.0, 0.98, 0.95, 0.90\}$ ,  $\Delta = 2000E_R$ ,  $\Gamma = 1000E_R$ ,  $\Omega_0 = 2000E_R$ .

$n + m$ . At these points both the smooth geometric potential and the scalar potential are maximum (see fig. 2), so it is energetically more favorable to have vortices centered there.

As the difference  $|1 - \nu|$  exceeds a critical value, it becomes more favorable for the ground state atoms to have vortices circulating around the narrow peaks of magnetic fluxes and the scalar potential corresponding to the zero points of  $\Omega_1$  with odd  $n + m$ . This leads to the reorganization of the ground state taking place for  $\nu = 0.9$  in Fig. 6. For the parameters used in Fig. 6, the value  $\nu = 0.9$  corresponds to the radius  $\rho_0 = \epsilon|1 - \nu|/k$  equal to the critical radius  $\rho_{c2}$  given by Eqs. (46)-(48), at which the atoms start feeling the narrow peaks of the scalar potential and effective magnetic field. The reorganization of the ground state is presented in Fig. 7, showing how the position of the vortex changes with  $\nu$  for various values of  $\epsilon$ . Around  $\epsilon = \nu = 1$  the vortices are located at the zero point of  $\Omega_1$  for even  $n + m$ . For larger values of  $1 - \nu$  the vortices become located around the Aharonov-Bohm spikes corresponding to the zero point of  $\Omega_1$  for odd  $n + m$ . By further increasing  $1 - \nu$ , the narrow peaks of the vector and scalar potential widen, so it becomes unfavorable for hosting there the vortices which return to the original position characteristic for  $\nu \approx 1$ . Note that reorganization of the Bloch states featured in Fig. 6 takes place before the bands touch each other and become topologically trivial.

The  $\Lambda$  scheme with the Rabi frequencies given by Eqs. (25)-(26) provides the topological subwavelength optical lattice of the square geometry. Such a scheme can be implemented if the ground states  $|1\rangle$  and  $|2\rangle$  are non-degenerate. Because of the energy difference between the atomic ground states, the optical transitions  $|1\rangle \rightarrow |e\rangle$  and  $|2\rangle \rightarrow |e\rangle$  can be individually accessed by the laser fields with the polarizations which are not necessarily well defined. The energy difference between the ground states can be achieved using two different hyperfine ground states or applying a strong bias magnetic field splitting the two hyperfine states with different spin



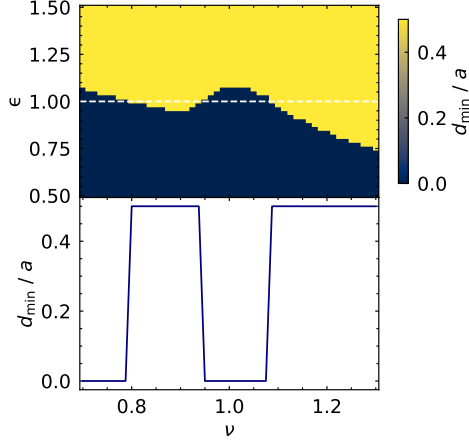


FIG. 7. Dependence on  $\epsilon$  and  $\nu$  of the position of the density dips for the lowest Bloch band. Here  $d_{\min}$  is the distance of the density dip from  $x = y = 0$  corresponding to the zero point of  $\Omega_1$  for even  $n + m$ . Around  $\epsilon = \nu = 1$  this distance is 0 (dark color). Beyond this area with the increase of  $|1 - \nu|$  the vortices become situated around the Aharonov-Bohm spikes corresponding to the distance  $d_{\min}$  equal to  $a/2$  (light color).

projections. The degeneracy of the two ground states would prevent realization of this setup because of the polarization constraint due to the transversality of the standing electromagnetic waves and the square geometry used. Note that a similar kind of the subwavelength topological lattice can be created using the  $\Lambda$  scheme with degenerate ground states for the triangular geometry of the light fields [18]. In that case, going beyond the fine tuned parameter regime considered in ref. [18], we have found that both the effective magnetic field and the geometric scalar potential exhibits then narrow and intense subwavelength peaks distributed in a hexagonal way. Away from these subwavelength spots, magnetic field changes the sign and becomes smooth, as in the square lattice. Topological subwavelength lattices of non-square geometry will be considered in more detail elsewhere.

### E. Existence of ideal Chern bands

There has been a considerable recent interest in simulating a fractional Chern insulator (FCI) using different platforms, including ultracold atoms [25, 30, 31]. While having a non-zero Chern number is a necessary condition for formation of FCI, it is not sufficient to stabilize the many-body FCI phase [32–34]. Thus the energy bands must satisfy certain conditions, which allow a mapping to Landau levels (LL). This can be studied via the quantum geometric tensor (QGT)  $\mathcal{Q}_{\mathbf{q}}^{ab}$ , which is defined as [35]:

$$\mathcal{Q}_{\mathbf{q}}^{ab} = \sum_{s \in \mathcal{S}} \langle \partial^a u_{\mathbf{q}s} | \hat{R}_{\mathbf{q}} | \partial^b u_{\mathbf{q}s} \rangle, \quad (49)$$

where the partial derivatives  $\partial^a$  and  $\partial^b$  are taken with respect to the quasi-momentum components  $q_a$  and  $q_b$ , with  $a, b \in \{q_x, q_y\}$ . Here  $|u_{\mathbf{q}s}\rangle$  is the periodic Bloch state vector at quasi-momentum  $\mathbf{q}$  for the  $s$ -th band,  $\mathcal{S}$  is the set of bands under consideration, the operator  $\hat{R}_{\mathbf{q}} = \hat{I} - \sum_{s \in \mathcal{S}} |u_{\mathbf{q}s}\rangle \langle u_{\mathbf{q}s}|$  projects onto the complement subspace and  $\hat{I}$  is the identity operator. No summation over  $s$  is to be taken if we are considering a geometric tensor just for a single Bloch band.

The form of QGT presented in Eq. (49) is not convenient for numerical calculations, as one would need a continuous phase gauge for the Bloch state vectors. Yet, one can express the QGT in terms of gauge-invariant projectors in the following way [35]:

$$\mathcal{Q}_{\mathbf{q}}^{ab} = \text{Tr} \left( \hat{P}_{\mathbf{q}} \left( \partial^a \hat{P}_{\mathbf{q}} \right) \left( \partial^b \hat{P}_{\mathbf{q}} \right) \right), \quad (50)$$

where  $\hat{P}_{\mathbf{q}} = \sum_{s \in \mathcal{S}} |u_{\mathbf{q}s}\rangle \langle u_{\mathbf{q}s}|$  is the projector onto the subspace of relevant Bloch bands.

Here we will use two well-established quasi-momentum space criteria for  $q$ -ideal Chern bands [33]:

(i) for all quasi-momenta in the Brillouin zone, the QGT has a constant null vector, i.e.,  $\mathcal{Q}_{\mathbf{q}}^{ab} w_b = 0$ , where the summation over the repeated index  $b$  is implied.

(ii) the integral  $D_{\text{QGT}} = \int_{1\text{BZ}} d^2 \mathbf{q} \det(\mathcal{Q}_{\mathbf{q}}^{ab})$  equals zero, i.e.,  $D_{\text{QGT}} = 0$ .

We find that for all quasi-momenta  $\mathbf{q}$  in the Brillouin zone, the quantum geometric tensor (QGT) possesses a null vector up to numerical accuracy (eigenvalues deviate from zero by  $\sim 10^{-4}$ ). For an ideal Chern band, the null vector  $\vec{w}_{\mathbf{q}}$  of QGT  $\vec{Q}_{\mathbf{q}}$  must be  $\mathbf{q}$ -independent across the entire Brillouin zone. To quantify the null vector's uniformity, we calculate its standard deviation from the averaged value  $\langle \vec{w}_{\mathbf{q}} \rangle$  given by:

$$\sigma_{\text{QGT}} = \frac{1}{A} \int_{1\text{BZ}} d^2 \mathbf{q} |\vec{w}_{\mathbf{q}} - \langle \vec{w}_{\mathbf{q}} \rangle|^2, \quad (51)$$

where  $A$  is the area of the first Brillouin zone (1BZ). A small value of the standard deviation,  $\sigma_{\text{QGT}} \ll 1$ , indicates a nearly constant null vector.

For parameter values near  $\epsilon = \nu = 1$ , we observe that the standard deviation  $\sigma_{\text{QGT}}$  is indeed much less than unity, it is below 0.1, as seen in Fig. 8(a). Away from the aforementioned parameter region, the null vector obtains a more significant  $\mathbf{q}$ -dependence and the condition (i) for an ideal Chern band is no longer satisfied. The condition (ii) also applies in a range of parameters around  $\epsilon = \nu = 1$ , as seen in Fig. 8(b), but covers a somewhat larger region of  $\epsilon$ - $\nu$  parameter space as compared to Fig. 8(a). It is noteworthy that in Subsec. IV D, Fig. 6, the reorganization of the ground state was observed around  $\nu = 0.95$  and  $\epsilon = 1$ , where a slight deviation from the optimal value of condition (i) is seen in Fig. 8(a).

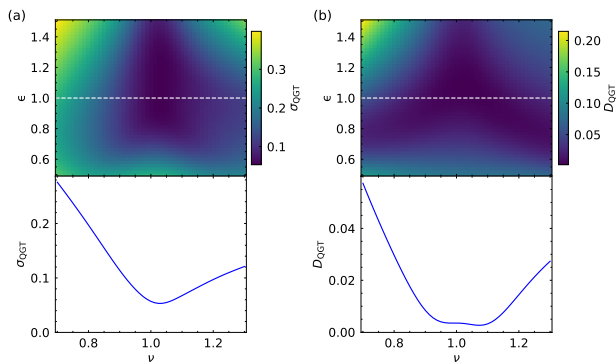


FIG. 8. Dependence on  $\epsilon$  and  $\nu$  of the standard deviation of the QGT null vector field  $\sigma_{\text{QGT}}$  of the lowest Bloch band for  $\Delta = 2000E_R$ ,  $\Gamma = 1000E_R$ ,  $\Omega_0 = 2000E_R$ .

## V. CONCLUDING REMARKS

We have developed a general framework for engineering 2D sub-wavelength topological optical lattices for dark-state atoms. By properly designing the spatial profiles of the laser fields coupling atomic internal states in a  $\Lambda$  scheme, one can generate Kronig-Penney-like subwavelength scalar potentials co-localised with intense, narrow synthetic magnetic flux tubes. The latter are compensated by a smooth background magnetic field of opposite sign, leading to zero net magnetic flux per unit cell, yet still enabling topologically nontrivial band structures. Thus there are some similarities with the Haldane-type lattice model [26] with zero net flux over an elementary cell, but non-trivial topology due to non-zero fluxes over the individual plaquettes constituting the elementary cell. Returning to the present situation, for narrow enough flux peaks, the atoms effectively experience a uniform background magnetic field, resembling the Landau level problem. This supports nearly flat Bloch bands with unit Chern numbers, like in the quantum Hall systems.

We also verified that the system supports ideal Chern bands, as both Quantum Geometric Tensor conditions—null vector constancy and vanishing determinant integral—are satisfied near the perfect tuning point where  $\epsilon$  and  $\nu$  are close to unity. This makes the scheme well-suited for simulating the fractional Chern insulators in ultracold atomic gases, offering a new platform for exploring strongly correlated topological phases with high tunability.

## ACKNOWLEDGEMENTS

G.J. thanks Jean Dalibard for helpful discussions on ref. [18]. The authors acknowledge support from the Lithuanian Research Council (Grant No. S- MIP-24-97). This work has also received funding from COST Action POLYTOPO CA23134, supported by COST (European

Cooperation in Science and Technology).

- 
- [1] M. Lewenstein, A. Sanpera, V. Ahufinger, B. Damski, A. Sen(De), and U. Sen, Ultracold atomic gases in optical lattices: mimicking condensed matter physics and beyond, *Advances in Physics*, **Adv. Phys.** **56**, 243 (2007).
- [2] I. Bloch, J. Dalibard, and W. Zwerger, Many-body physics with ultracold gases, *Rev. Mod. Phys.* **80**, 885 (2008).
- [3] O. Dutta, M. Gajda, P. Hauke, M. Lewenstein, D.-S. Lühmann, B. A. Malomed, T. Sowiński, and J. Zakrzewski, Non-standard hubbard models in optical lattices: a review, *Reports on Progress in Physics* **78**, 066001 (2015).
- [4] C. Gross and I. Bloch, Quantum simulations with ultracold atoms in optical lattices, *Science* **357**, 995 (2017).
- [5] F. Schäfer, T. Fukuhara, S. Sugawa, Y. Takasu, and Y. Takahashi, Tools for quantum simulation with ultracold atoms in optical lattices, *Nature Reviews Physics* **2**, 411 (2020).
- [6] M. O. Scully and M. S. Zubairy, *Quantum optics* (Cambridge University Press, 1997).
- [7] N. V. Vitanov, A. A. Rangelov, B. W. Shore, and K. Bergmann, Stimulated raman adiabatic passage in physics, chemistry, and beyond, *Rev. Mod. Phys.* **89**, 015006 (2017).
- [8] J. Dalibard, F. Gerbier, G. Juzeliūnas, and P. Öhberg, Colloquium: Artificial gauge potentials for neutral atoms, *Rev. Mod. Phys.* **83**, 1523 (2011).
- [9] N. Goldman, G. Juzeliūnas, P. Öhberg, and I. B. Spielman, Light-induced gauge fields for ultracold atoms, *Rep. Prog. Phys.* **77**, 126401 (2014).
- [10] M. Łacki, M. A. Baranov, H. Pichler, and P. Zoller, Nanoscale "dark state" optical potentials for cold atoms, *Phys. Rev. Lett.* **117**, 233001 (2016).
- [11] F. Jendrzejewski, S. Eckel, T. G. Tiecke, G. Juzeliūnas, G. K. Campbell, L. Jiang, and A. V. Gorshkov, Subwavelength-width optical tunnel junctions for ultracold atoms, *Phys. Rev. A* **94**, 063422 (2016).
- [12] W. Ge and M. S. Zubairy, Dark-state optical potential barriers with nanoscale spacing, *Phys. Rev. A* **101**, 023403 (2020).
- [13] P. Kubala, J. Zakrzewski, and M. Łacki, Optical lattice for a tripodlike atomic level structure, *Phys. Rev. A* **104**, 053312 (2021).
- [14] E. Gvozdiavas, P. Račkauskas, and G. Juzeliūnas, Optical lattice with spin-dependent sub-wavelength barriers, *SciPost Phys.* **11**, 100 (2021).
- [15] Y. Wang, S. Subhankar, P. Bienias, M. Łacki, T.-C. Tsui, M. A. Baranov, A. V. Gorshkov, P. Zoller, J. V. Porto, and S. L. Rolston, Dark state optical lattice with a subwavelength spatial structure, *Phys. Rev. Lett.* **120**, 083601 (2018).
- [16] T.-C. Tsui, Y. Wang, S. Subhankar, J. V. Porto, and S. L. Rolston, Realization of a stroboscopic optical lattice for cold atoms with subwavelength spacing, *Phys. Rev. A* **101**, 041603(R) (2020).
- [17] E. Gvozdiavas, I. B. Spielman, and G. Juzeliūnas, Interference-induced anisotropy in a two-dimensional dark-state optical lattice, *Phys. Rev. A* **107**, 033328 (2023).
- [18] S. Nascimbene and J. Dalibard, *Emergence of a landau level structure in dark optical lattices* (2024), [arXiv:2412.15038 \[cond-mat.quant-gas\]](https://arxiv.org/abs/2412.15038).
- [19] T. Hernández Yanes, M. Płodzień, M. Mackoīt Sinkevičienė, G. Žlabys, G. Juzeliūnas, and E. Witkowska, One- and two-axis squeezing via laser coupling in an atomic fermi-hubbard model, *Phys. Rev. Lett.* **129**, 090403 (2022).
- [20] R. Dum and M. Olshanii, Gauge structures in atom-laser interaction: Bloch oscillations in a dark lattice, *Phys. Rev. Lett.* **76**, 1788 (1996).
- [21] G. Juzeliūnas, J. Ruseckas, and P. Öhberg, Effective magnetic fields induced by EIT in ultra-cold atomic gases, *J. Phys. B: At. Mol. Opt. Phys.* **38**, 4171 (2005).
- [22] G. Juzeliūnas, J. Ruseckas, and P. Öhberg, Effective magnetic fields induced by eit in ultra-cold atomic gases, *Journal of Physics B: Atomic, Molecular and Optical Physics* **38**, 4171 (2005).
- [23] G. Juzeliūnas and I. B. Spielman, Flux lattices reformulated, *New. J. Phys.* **14**, 123022 (2012).
- [24] N. R. Cooper, Optical flux lattices for ultracold atomic gases, *Phys. Rev. Lett.* **106**, 175301 (2011).
- [25] N. R. Cooper and J. Dalibard, Reaching fractional quantum hall states with optical flux lattices, *Phys. Rev. Lett.* **110**, 185301 (2013).
- [26] F. D. M. Haldane, Model for a quantum hall effect without landau levels: Condensed-matter realization of the "parity anomaly", *Phys. Rev. Lett.* **61**, 2015 (1988).
- [27] C.-K. Chiu, J. C. Y. Teo, A. P. Schnyder, and S. Ryu, Classification of topological quantum matter with symmetries, *Rev. Mod. Phys.* **88**, 035005 (2016).
- [28] Y. Braver, D. Burba, S. S. Nair, G. Žlabys, E. Anisimovas, T. Busch, and G. Juzeliūnas, *Light-induced localized vortices in multicomponent bose-einstein condensates* (2025), [arXiv:2506.08683 \[cond-mat.quant-gas\]](https://arxiv.org/abs/2506.08683).
- [29] We have calculated the Chern numbers  $c$  of the Bloch bands using the algorithm presented by T. Fukui, Y. Hatsugai, and H. Suzuki, *J. Phys. Soc. Jpn.* **74**, 1674 (2005).
- [30] J. Léonard, S. Kim, J. Kwan, P. Segura, F. Grusdt, C. Repellin, N. Goldman, and M. Greiner, Realization of a fractional quantum hall state with ultracold atoms, *Nature* **619**, 495 (2023).
- [31] P. Lunt, P. Hill, J. Reiter, P. M. Preiss, M. Gałka, and S. Jochim, Realization of a Laughlin state of two rapidly rotating fermions, *Physical Review Letters* **133**, 253401 (2024).
- [32] J. Wang, J. Cano, A. J. Millis, Z. Liu, and B. Yang, Exact Landau level description of geometry and interaction in a flatband, *Phys. Rev. Lett.* **127**, 246403 (2021).
- [33] B. Estienne, N. Regnault, and V. Crépel, Ideal Chern bands as Landau levels in curved space, *Phys. Rev. Res.* **5**, L032048 (2023).
- [34] P. J. Ledwith, A. Vishwanath, and D. E. Parker, Vortexability: A unifying criterion for ideal fractional Chern insulators, *Phys. Rev. B* **108**, 205144 (2023).
- [35] J. Mitscherling, A. Avdoshkin, and J. E. Moore, *Gauge-invariant projector calculus for quantum state geometry and applications to observables in crystals* (2025), [arXiv:2412.03637 \[cond-mat.str-el\]](https://arxiv.org/abs/2412.03637).